Volume 27, issue 2, March 2009 ISSN 0263-4368

International Journal of
REFRACTORY METALS & HARD MATERIALS

SPECIAL ISSUE: INTERNATIONAL CONFERENCE ON THE SCIENCE OF HARD MATERIALS–9

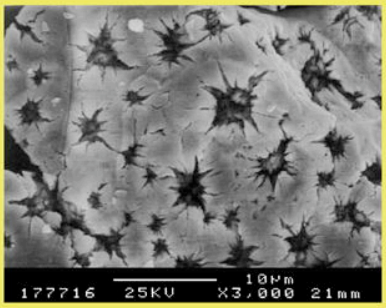

Int. Journal of Refractory Metals & Hard Materials 27 (2009) 458–464

Contents lists available at ScienceDirect

Int. Journal of Refractory Metals & Hard Materials

journal homepage: www.elsevier.com/locate/IJRMHM

Microtexture and hardness of CVD deposited α-Al_2O_3 and TiC_xN_{1-x} coatings

Harry Chien [a], Michael C. Gao [a], Herbert M. Miller [a], Gregory S. Rohrer [a,*], Zhigang Ban [b], Paul Prichard [b], Yixiong Liu [b]

[a] Department of Materials Science and Engineering, Carnegie Mellon University, 5000 Forbes Avenue, Pittsburgh, PA 15213, USA
[b] Kennametal Incorporated, 1600 Technology Way, P.O. Box 231, Latrobe, PA 15650, USA

ARTICLE INFO

Article history:
Received 23 August 2008
Accepted 1 September 2008

Keywords:
Coatings
Microstructure
Texture
Hardness

ABSTRACT

The microstructures of chemical vapor deposited coatings on four tool inserts have been comprehensively characterized using electron backscatter diffraction mapping. Nanoindentation was used to measure the hardness of the TiC_xN_{1-x} and α-Al_2O_3 layers in each coating. The TiC_xN_{1-x} layers have weak [1 1 2] or [1 0 1] textures in the growth direction and are highly twinned. In these layers, coherent twins make up 13%–20% of the total grain boundary length. The alumina layers have $[10\bar{1}4]$ or [0 0 0 1] textures in the growth direction that are 4.2–8.8 times random. The hardest coatings consist of highly twinned TiC_xN_{1-x} layers with weak [1 1 2] texture and α-Al_2O_3 with strong $[10\bar{1}4]$ texture.

1. Introduction

Many of the cemented carbide cutting tool inserts used today have multilayer coatings that enhance their performance, durability, and wear resistance. These coatings have a wide range of structures and compositions and can be deposited by physical vapor deposition or chemical vapor deposition (CVD). In the present paper, we focus on TiC_xN_{1-x} ||α-Al_2O_3||TiN coatings deposited by CVD, where $0.3 < x < 0.5$. In these coatings, the TiC_xN_{1-x} and α-Al_2O_3 layers are each less than 10 µm thick and the TiN capping layer is approximately 1 µm thick. These coatings are representative of the most commonly used coatings in the US and western Europe [1].

Coatings on cutting tool inserts are deposited at elevated temperature and differential thermal expansion during cooling usually leads to the formation of vertical cracks and weak residual tensile stresses [1]. Early studies of structure property relationships in these coatings have shown that these films usually have columnar grain structures and that reduced grain sizes were associated with increased microhardness and abrasive wear resistance [2]. The hardness exhibits an approximate Hall–Petch relationship with the grain size [2]. The effect of crystallographic texture in the coatings is less well understood. Existing data on texture has been derived from X-ray diffraction and, for example, it has been reported that the TiC_xN_{1-x} layer in certain coatings has weak [2 2 0] texture [3]. Other moderate temperature CVD TiC_xN_{1-x} coatings have been reported to have twinned, columnar microstructures with [1 1 2] texture [4]. The alumina films can be prepared with a range of textures and is has been shown that coatings with $[10\bar{1}4]$ texture have superior wear resistance [5–7].

The goal of the present paper is to comprehensively characterize the microstructures of four coated tool inserts to see if the microstructural characteristics can be related to measured hardness values. Orientation maps derived from electron backscatter diffraction (EBSD) data are used to measure the grain sizes and shapes, the distribution of grain orientations, and the distribution of grain boundary misorientations. Hardness values are obtained from nanoindentation experiments. We find that the TiC_xN_{1-x} layers have weak [1 1 2] or [1 0 1] textures and a very high population of twins. The alumina layers have relatively stronger texture with preferred $[10\bar{1}4]$ or [0 0 0 1] orientations. There are no dominant correlations between the hardness and the grain size or the hardness and microtexture. However, the hardest alumina coatings have $[10\bar{1}4]$ orientation texture and small grain sizes. The hardest TiC_xN_{1-x} coatings have a small grain sizes, [1 1 2] texture, and a high density of twins.

2. Experimental details

The tool inserts were ground and polished in two ways to allow for both microstructural characterization and hardness measurements (see Fig. 1). The first section plane, labeled 1, creates a cross section of the insert so that each component of the multilayer coating can be observed perpendicular to the growth direction. Note that the reference frames for the images of the cross sections, in Figs. 2, 4a, and 5, are rotated by 90°, clockwise, with respect to Fig. 1c. The second section plane, labeled 2 in Fig. 1b, was polished

* Corresponding author.
E-mail address: rohrer@cmu.edu (G.S. Rohrer).

0263-4368/$ - see front matter © 2008 Elsevier Ltd. All rights reserved.
doi:10.1016/j.ijrmhm.2008.09.010

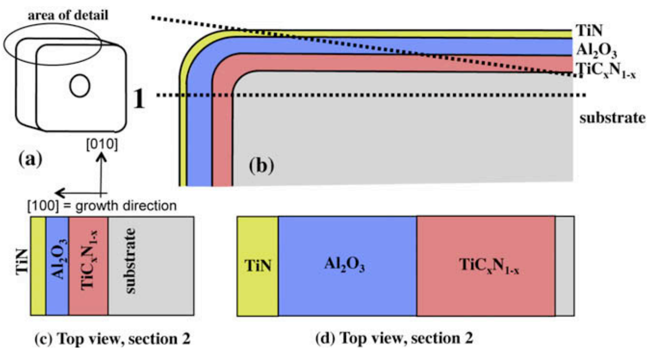

Fig. 1. Schematic illustration of the geometries of the sections used to study the tool inserts. (a) Macroscopic structure of the insert, with the area of interest marked by an oval. (b) Cross section illustrating the two section planes, labeled 1 and 2 and marked by dashed lines. Note that the dimensions of features in this schematic are exaggerated for clarity and not to scale. (c) Schematic view of the coating in cross section and (d) the low angle polish used for the hardness measurements.

at an approximate angle of 2° with respect to the surface of the coating so that when viewed from the top, extended regions of each layer are visible, as depicted in Fig. 1d. Both sections were prepared by first grinding with abrasives from 200 to 1600 grit size, then by polishing with 3 µm and 0.5 µm alumina slurries.

Grain orientation measurements by EBSD were challenging because of charging. Without a conductive coating, the EBSD patterns were unsatisfactory for indexing. On the other hand, if the coating is too thick, the surface of interest is obscured. The ideal carbon coatings were deposited in a vacuum of 0.7×10^{-1} atm from a heated carbon filament. The carbon fiber was preheated with constant power for 1 s, and then a pulsed signal was applies for 5 s to deposit the coating.

All EBSD maps were measured using an orientation imaging microscopy (OIM) system (EDAX, Inc.) incorporated in a Phillips XL40 FEG scanning electron microscope (SEM). The samples were tilted to an angle of 60° with respect to the beam and patterns were recorded using an accelerating voltage of 20 kV. Orientation data were recorded at spatial intervals of 50 nm for samples 1 and 2 and 100 nm for samples 3 and 4. The data were processed and analyzed using OIM software version 4.6. The grain orientation data was processed to remove spurious observations using the 'grain dilation clean-up' procedure in the software. In this process, the grain tolerance angle was fixed at 5° and the minimum grain size was set at 12 pixels. Finally, the orientations within each grain were averaged so that there was a single orientation per grain. To obtain suitable statistics for the texture analysis, multiple adjacent images were collected along the length of the exposed films. The data sets for the $TiC_{1-x}N_x$ layers were made up of at least 2000 grains. For the alumina layers, the data sets were made up of at least 560 grains (see Table 1 for details). Data sets of this size are sufficient to determine the texture with greater than 90% confidence [8].

The OIM analysis software was then used to extract more than 5000 boundary line traces from each TiC_xN_{1-x} layer. The grain boundary segments in each sample are classified in the following way. If the misorientation is within Brandon's [9] criterion (8.7°) of the ideal $\Sigma3$ misorientation (60° of disorientation about the [1 1 1] axis), and the surface trace of the boundary is within 10° of orientation of the coherent twin (both grains terminated by (1 1 1) planes), it is classified as a coherent twin. If the misorientation is within Brandon's criterion of the ideal $\Sigma3$ misorientation, but the surface trace of the boundary is more than 10° from the orientation of the coherent twin, then it is classified as an incoherent $\Sigma3$. If the boundary does not meet the Brandon criterion, it is considered a random boundary. It should be noted that some of the

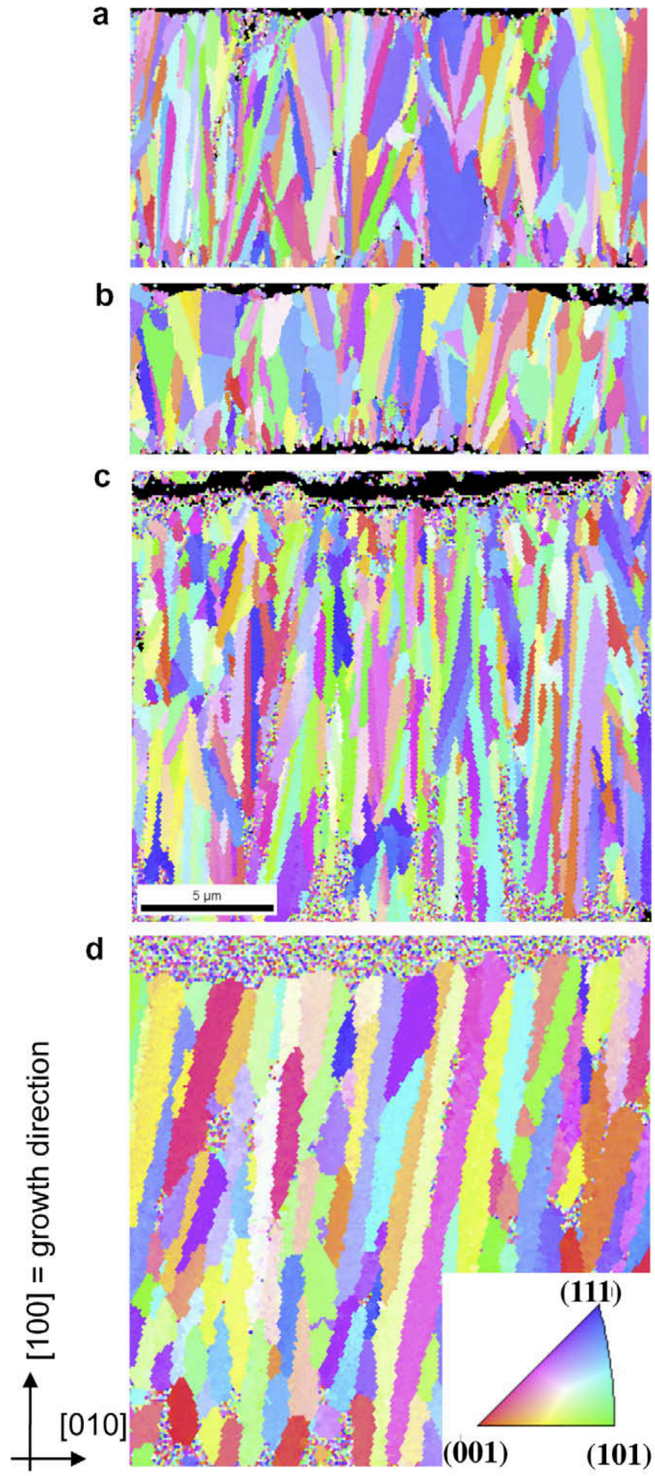

Fig. 2. Inverse pole figure maps for the TiC_xN_{1-x} layers in (a) sample 1, (b) sample 2, (c) sample 3, and (d) sample 4. Each color corresponds to a crystal orientation, defined in the inset key. The scale in (c) is the same in all three maps.

incoherent $\Sigma3$s have traces that are coincidentally within the 10° tolerance and will be incorrectly classified as coherent. This leads to a small overestimation of the coherent twin population and an underestimation of the incoherent $\Sigma3$ population.

The greatest number of line segments (22,420) were extracted from sample 1 and these were used to calculate the grain boundary plane distribution for the $\Sigma3$ misorientation using a procedure described previously [10,11]. It should be noted that while the data

Table 1
Summary of Microstructural Characteristics and Hardness for Coatings

Layer	Sample	Grains	Grain area (μm^2)	Major axis (μm)	Minor axis (μm)	Texture orientation/MRD	Mean hardness, (GPa)
$TiC_{1-x}N_x$	1	5538	2.1	4.85	0.67	{112} 1.4	21.8 (0.8)
	2	1112	1.6	3.46	0.69	{112} 1.5	20.8 (1.0)
	3	1996	1.93	4.83	0.54	{112} 1.9	21.7 (0.7)
	4	2050	3.34	5.03	0.79	{101} 3.1	20.3 (0.7)
Al_2O_3	1	950	2.05	3.08	0.84	$\{10\bar{1}4\}$ 8.8	24.6 (2.2)
	2	2567	3.9	3.36	1.36	$\{10\bar{1}4\}$ 4.2	24.2 (1.3)
	3	1151	3.95	4.79	0.99	{0001} 6.8	22.3 (1.2)
	4	568	3.89	4.34	1.07	{0001} 5.2	21.1 (1.4)

set is not extensive enough to determine the grain boundary plane distribution at all misorientations, there are more than 3400 traces from $\Sigma 3$ grain boundaries so the plane distribution at this particular misorientation is reliable.

The grain shapes and sizes were analyzed using Image J, a program developed by National Institutes of Health [12]. In this analysis, grains from the orientation maps are fitted to ideal elliptical shapes and the geometric properties of these ellipses are then calculated to determine the average area and the average dimensions of the major and minor axes.

Hardness measurements were made using a nanoindenter XP (MTS systems corporation) equipped with a Berkovich diamond tip. The diamond tip was calibrated using measurements on fused silica. The hardness and modulus were determined using the standard practice for instrumented indentation testing [13]. For all of the measurements, the indenter approach rate was 25 nm/s. Once the indenter contacted the surface, the load on the sample increased to a maximum of 10 mN within the time span of 25 s. The maximum load was then held constant for 10 s. Finally, the indenter was withdrawn at twice the loading rate. The maximum depth of indentation was 2 μm. Indentations on coatings invariably probe both the top layer and the underlying layers. In an attempt to assess the influence of the underlayers, samples were polished at an $\sim 2°$ angle with respect to the substrate orientation. When moving laterally across the surface from the substrate to the topmost layer, the sequential indents probe progressively thicker layers. At each position, 10–15 indents were made and the values reported are the means and standard deviations of these measurements.

3. Results

Inverse pole figure maps for the TiC_xN_{1-x} layers are shown in Fig. 2. Note that the growth direction is vertical. The grain colors correspond to the orientations defined in the key. Black areas and areas with speckled contrast at the tops and bottoms of the maps represent areas where patterns were not indexed. With a step size of 50 nm and a minimum grain size of 12 pixels, grains with diameters smaller than 200 nm cannot be detected, so the fine grained transition regions at the tops and bottoms appear black or as discrete speckled orientations. Within the bulk of the films, the grains are columnar in shape and are aligned along the growth axis. Average grain areas and the average dimensions of the major and minor elliptical axes are summarized in Table 1. Sample 3 has the highest aspect ratio ($\sim$9) and Sample 2 has the lowest ($\sim$5). However, it should be noted that the minor elliptical axis is essentially the same in samples 1 and 2; the greater aspect ratio of the grains in sample 1 derives from the fact that the coating is thicker and, therefore, the average major elliptical axis is longer.

Inverse pole figures for the TiC_xN_{1-x} layers are shown in Fig. 3. These figures are drawn with respect to the growth direction, [100]. Therefore, they show the relative frequency of crystal plane normals that are parallel to the growth direction, in multiples of a random distribution (MRD) units. All of the textures are relatively weak and all of the peaks indicate a preference for orientations that are perpendicular to the [111] direction, along the arc of the great circle that connects [112] to [101]. In samples 1 and 2, there is a nearly continuous distribution along this arc. In sample 3, the peak is more concentrated at the [112] orientation and in sample 4 it is concentrated at the [101] orientation. For simplicity, the textures in sample 1 and 2 are referred to as [112], the position of the maximum, even though there is actually a range of preferred orientations.

Inspection of the misorientation distribution function for the TiC_xN_{1-x} coatings (not shown) revealed a strong peak for the misorientation of 60° about the [111] axis. In coincident site lattice notation, this is a $\Sigma 3$ grain boundary. In the case that both planes on either side of the grain boundary are (111), this is a coherent twin. The image in Fig. 4a shows the microstructure of sample 1 (these are the same data as in Fig. 2a), where the contrast corresponds to the image quality associated with the EBSD patterns. Therefore, there is relatively lighter contrast within the grains and darker contrast at the grain boundaries. Those grain boundaries that have a $\Sigma 3$ misorientation are marked by red lines. More often than not, these lines are straight. We find that 28% of all the grain boundary length is of the $\Sigma 3$ type and that 20% of all grain boundary length has both the $\Sigma 3$ misorientation and has trace orientations that are consistent with the coherent twin. This is reflected in the distribution of grain boundary planes illustrated in Fig. 4b. The peak at the (111) position (of 760 MRD) shows that there are many more twins than one would expect if grain boundaries occurred randomly. The twin content, as a fraction of grain boundary length, is higher in sample 1 than in the other samples. The twin population in each of the samples was analyzed and the results are summarized in Table 2.

Inverse pole figure maps for the α-Al_2O_3 layers are shown in Fig. 5. Once again, the grains are columnar in shape and are aligned along the growth axis. The aspect ratios of these grains are smaller than for those in the TiC_xN_{1-x} layer. The grains in sample 3 appear to be the most columnar and have higher aspect ratios, while those in sample 2 are the most equiaxed. The one common feature among these coatings is the apparent texture. Based on the grain coloring, there is an obvious preference for prismatic grain orientations.

The inverse pole figures for the alumina layers in Fig. 6 show relatively strong textures. Once again, these figures are plotted with reference to the growth direction and indicate that the [0001] crystal axis is approximately aligned with the growth direction. For samples 1 and 2, the peak of the distribution is actually inclined with respect to [0001] and is more accurately described as $[10\bar{1}4]$. X-ray diffraction measurements of sample 1 were consistent with this assignment (although it should be mentioned that the angle between [0001] and $[10\bar{1}4]$ is approximately 5°). On the other hand, for samples 3 and 4, the preferred orientation is [0001]. Furthermore, it should be noted that the intensity of

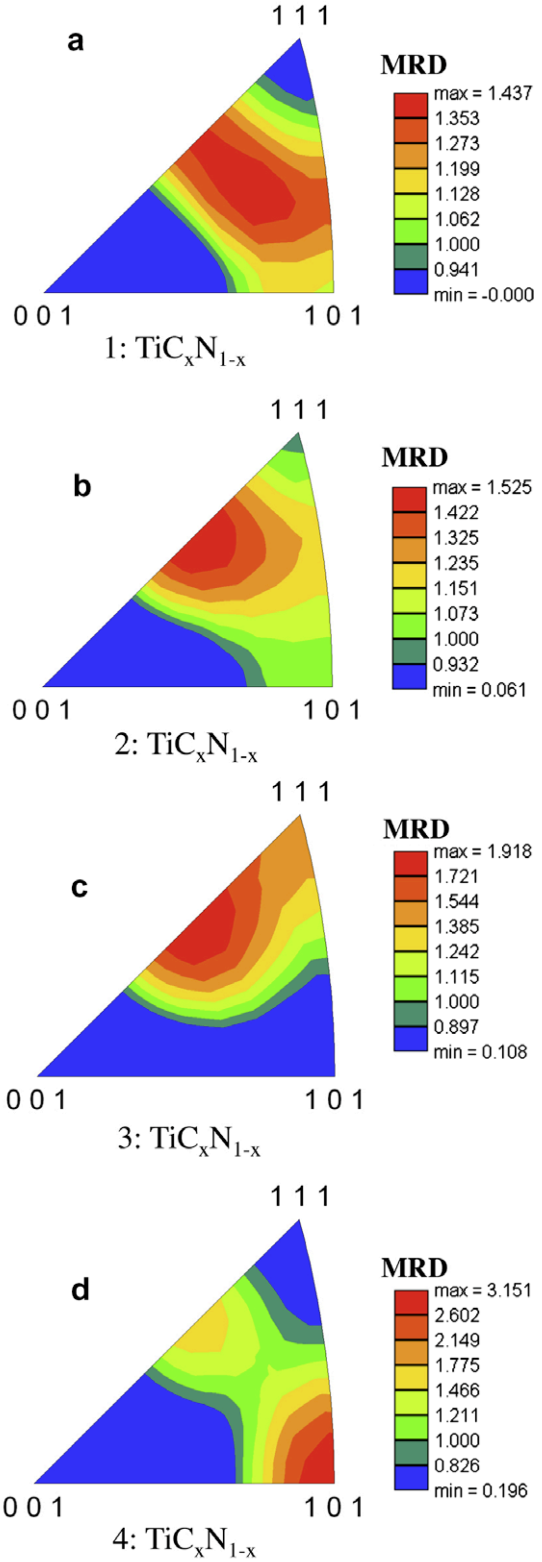

Fig. 3. Inverse pole figures for the TiC$_x$N$_{1-x}$ layers (a) sample 1, (b) sample 2, (c) sample 3, and (d) sample 4 with [1 0 0] (the growth direction) as the reference.

texture differs in the different specimens. Sample 1 has the strongest texture, sample 2 has the weakest texture, and samples 3 and 4 have intermediate values.

Hardness measurements were conducted on samples polished at an ~2° angle, as illustrated in Fig. 1d, and the results are shown in Fig. 7. The image at the top of the figure is a montage of optical micrographs of sample 1, recorded after the hardness measurements. Each phase in the coating has a distinct appearance and the location of the indent confirms the origin of the hardness data. Here we will attempt to interpret only the data from the TiC$_x$N$_{1-x}$ layer (positions 4, 5, and 6) and the α-Al_2O_3 layer (positions 8, 9 and 10). The values at each of these two sets of positions were averaged to determine the mean values of hardness reported in the final column of Table 1. With few exceptions, mean hardness values from comparable positions on different coatings do not differ by more than a standard deviation. However, there are clear trends in the mean values that appear to be significant. For example, the hardness values for the alumina layer of sample 1 are always larger than those of samples 3 and 4. In the next section, we attempt to draw correlations between these trends and the characteristics of the microstructure.

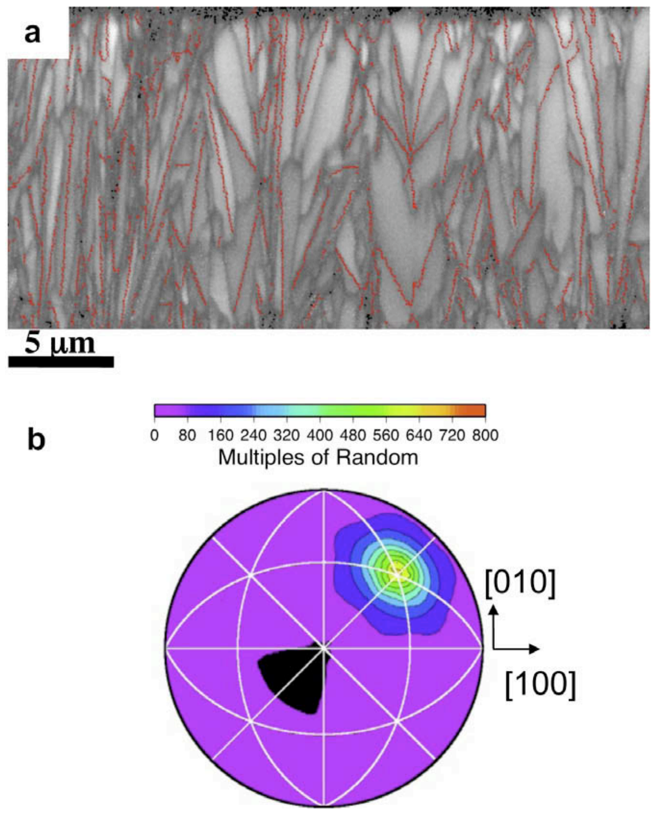

Fig. 4. (a) Image quality map of the TiC$_x$N$_{1-x}$ layer in sample 1. Dark contrast corresponds to poor image quality that is characteristic of patterns recorded at grain boundaries. The red lines denote Σ3 type grain boundaries. (b) The distribution of grain boundary planes for the Σ3 grain boundaries. The distribution is plotted on a stereographic projection. The peak is at the position of the misorientation axis, [1 1 1], indicates a high fraction of pure twist grain boundaries with (1 1 1) planes on either side of the boundary. This geometry corresponds to the coherent twin.

4. Discussion

The coatings examined in this work have a range of microstructural characteristics and this variability makes it possible to test ideas about the links between coating structure and coating properties. One interesting feature of the microstructure of the TiC$_x$N$_{1-x}$ layers is the high density of twins. This observation is consistent with the TEM results reported earlier [4]. The scope of the current measurements allows us to quantify the twin content of different films. This analysis reveals an inverse correlation between the fractional length of the twins and the strength of the texture; the strength of the texture is highest in sample 4, which also has the

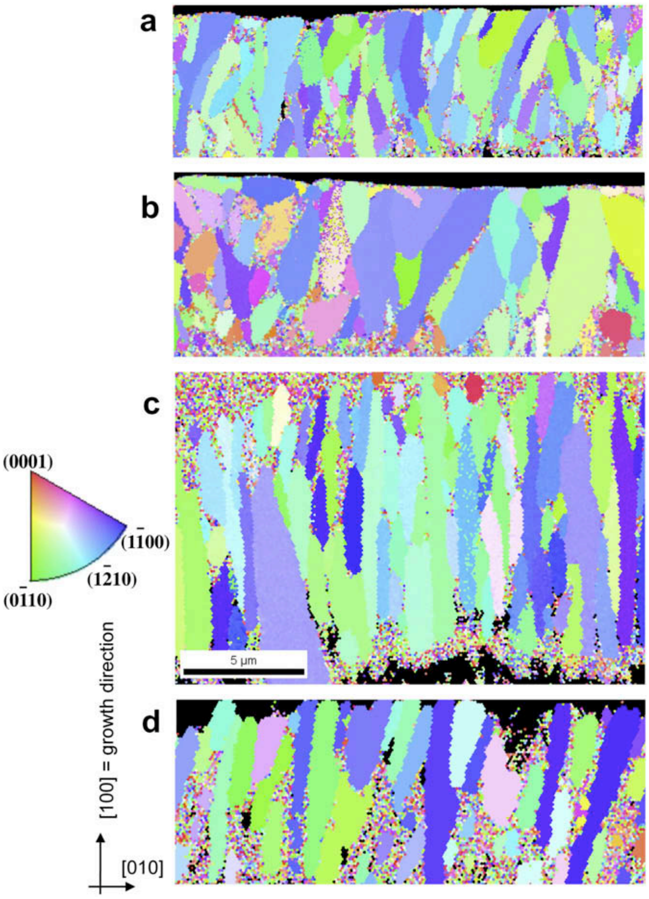

Fig. 5. Inverse pole figure maps for the α-Al_2O_3 layers in (a) sample 1, (b) sample 2, (c) sample 3, and (d) sample 4. Each color corresponds to a crystal orientation, defined in the key to the left. The scale in (c) is the same in all three maps.

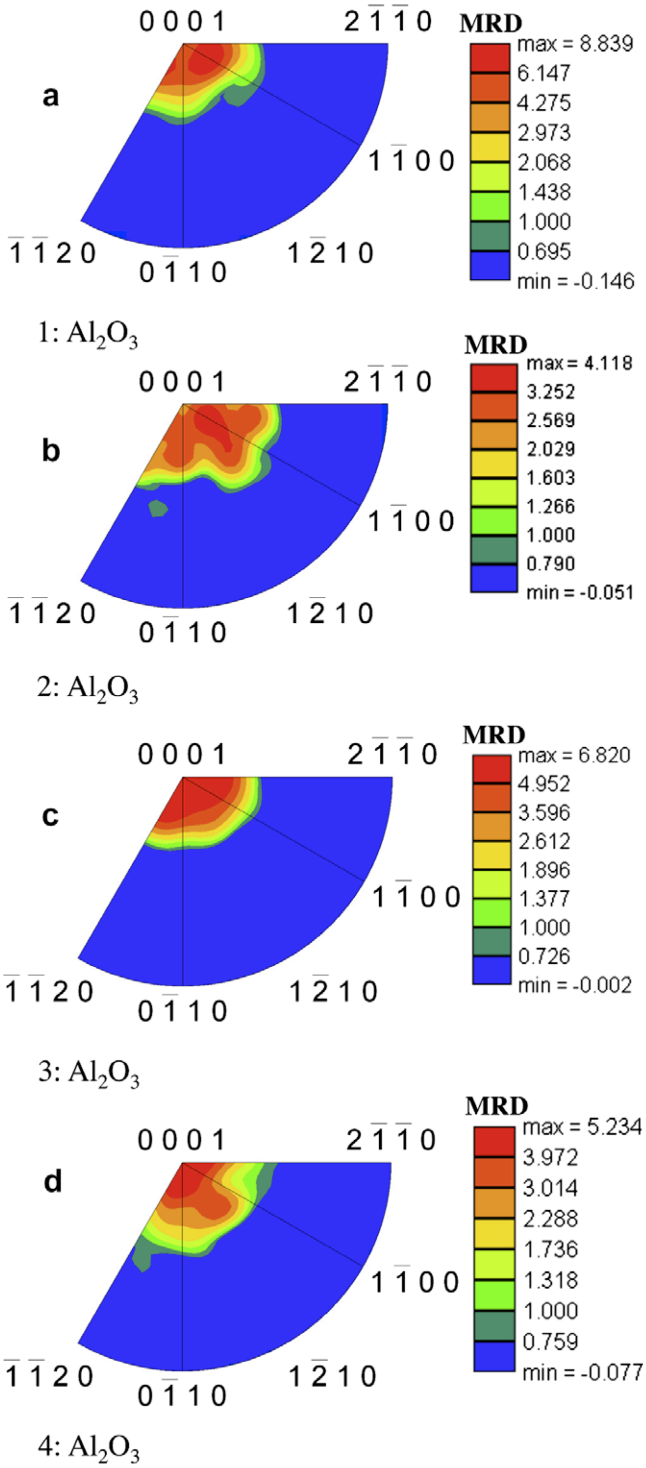

Fig. 6. Inverse pole figures for the α-Al_2O_3 layers. (a) sample 1, (b) sample 2, (c) sample 3, and (d) sample 4 with [1 0 0] (the growth direction) as the reference.

Table 2
Twin Populations in TiC_xN_{1-x} coatings

Sample	Number statistics%			Length statistics%		
	Non-Σ3	Σ3	Twins	Non-Σ3	Σ3	Twins
1	84	15	6	72	28	20
2	86	14	7	75	25	19
3	84	16	7	80	20	13
4	83	16	5	77	23	13

fewest twins. Twins tend to randomize the texture because if one grain takes the preferred orientation, the twinned grain is necessarily misoriented by 60°.

There is also an interesting relationship between the twinning and the spreading of the preferred orientations along the [1 1 1] zone. Because most of the twin boundaries are parallel to the growth direction, and these boundaries have (1 1 1) orientations in the crystal reference frame, the adjoining crystal orientations with respect to the growth direction must be perpendicular to [1 1 1], which places them in the [1 1 1] zone. This suggests a reason for the spreading of orientations along the [1 1 1] zone, especially in samples 1 and 2. It also suggests that the crystals must originally nucleate with orientations in the [1 1 1] zone, such as [1 0 1] or [1 1 2], and that twins grow from these nuclei.

One issue in evaluating the hardness of the different layers is that the underlying substrate and other layers necessarily influence the measurement. In the measurements presented in Fig. 7, the coating has a different thickness at each location. For example, at position 4, the TiC_xN_{1-x} layer is the thinnest and will be most strongly influenced by the substrate. At position 6, on the other hand, the layer is the thickest and the least influenced by the substrate. In all cases, the substrate has a lower hardness than the TiC_xN_{1-x}, so it is interesting that the hardness rises to its highest value when the layer is thin and decreases as the TiC_xN_{1-x} layer gets thicker at positions 5 and 6. A plausible reason for this is that the grains in the thinner region are smaller than those in the thicker region and, therefore, the film is harder. The grains are obviously

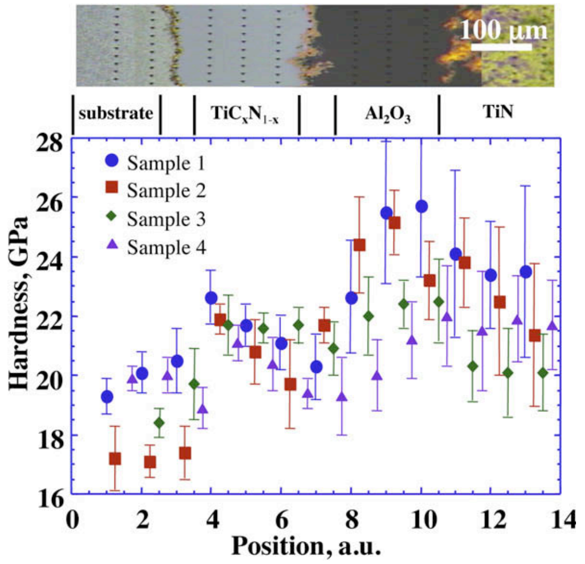

Fig. 7. Measured hardness values across section 2 as a function of position (see Fig. 1d) for sample 1 (circles), sample 2 (squares), sample 3 (diamonds), and sample 4 (triangles). Each data set is offset along the x-axis by 0.25 to minimize overlap of the data. The symbols represent mean values and the bars show ± one standard deviation. Above the graph is a montage of optical micrographs showing the location of the indents in sample 1. The vertical rows of black spots are the multiple indents used to determine the mean and standard deviation of the hardness and the different regions are labeled.

smaller along the major elliptical axis, because part of the coating has been removed. They are also smaller along the minor elliptical axis because the grains are smaller in the nucleation layer and generally become wider as the film gets thicker (see Fig. 2). To test this idea, the microstructure of the TiC_xN_{1-x} layer of sample 1 was divided into three layers of equal thickness and ellipses were fit to the grain in each of these sublayers. For the portion closest to the substrate, where the hardness is the highest (22.6 GPa), the average grain area was 0.2 μm^2. For the middle region it was 0.24 μm^2 and for the region furthest from the substrate, where the hardness was the lowest (21.1 GPa), it was 0.27 μm^2. The hardness tends to increase with thickness in the alumina layer (positions 8 through 10 in Fig. 7), as one would expect for a hard layer on a relatively softer layer.

One of the microstructural characteristics that can be expected to influence the hardnesses of the coatings is the grain size, by the well-known Hall-Petch effect. Because these coatings are columnar, the average length of the major elliptical axis is principally determined by the thickness of the coating. As there is no obvious relationship between the thickness of the film and its hardness, we assume that it is the dimension of the minor elliptical axis that is important. For the TiC_xN_{1-x} layer, the coating with the largest minor axis (4) does have the lowest mean hardness. However, the coating with the smallest average minor axis (3) has a hardness comparable to sample 1, which has a somewhat larger grain size. It should be noted that the variation in the TiC_xN_{1-x} hardness among the coatings is not as great the thickness dependence within a single coating. For the alumina layer, the differences in the hardnesses of the coatings are more significant. Once again, the hardest coating has the smallest grain size, but only three of the four observations follow the expected correlation between grain size and hardness. These observations suggest that there are factors other than the grain size that are influencing the hardness of these coatings.

A second microstructural characteristic that can influence hardness is the texture. For example, the effective elastic modulus is different along different directions. If the material is textured with soft or stiff directions perpendicular the growth surface, the hardness of the film will be influenced. For materials with anisotropic thermal expansion, such as alumina, thermal stresses are very sensitive to the texture and such stresses can also influence the hardness of coatings. In general, increased texture leads to a reduction in the level of thermal stresses [14,15]. Therefore, both the strength of the texture and the orientation are potentially important parameters. In the data presented here, there is no apparent correlation between the strength of the texture and the hardness. Instead, the notable trend appears to be with the type of texture. For the TiC_xN_{1-x} layer, the softest layer is the one exhibiting [1 0 1] texture and the harder ones have [1 1 2] textures. For the alumina layers, the two layers with $[1 0 \bar{1} 4]$ texture are harder than those with [0 0 0 1]. It is noteworthy that in previous work, this was the texture that was found to exhibit superior wear resistance [6].

Finally, it is worth commenting on the possible role of twins in the microstructure. Twin grain boundaries have compact atomic structures and very low energies. Therefore, they are expected to resist grain boundary fracture more than general boundaries and this may lead to higher hardness. While once again there is no distinct trend, the hardest TiC_xN_{1-x} layer has the highest twin density and the softest TiC_xN_{1-x} layer has the lowest twin density. Therefore, it is possible that the twins make a positive contribution to the coating hardness. If so, there is an interesting parallel with FCC structured metals and alloys where it has been demonstrated that higher densities of twins leads to improved resistance to corrosion and mechanical damage [16].

5. Conclusion

The microstructures of four CVD deposited coatings have been comprehensively characterized. The TiC_xN_{1-x} layers are highly twinned, with coherent twins making up 13%–20% of the grain boundary length. The alumina layers have $[1 0 \bar{1} 4]$ or [0 0 0 1] textures that are 4.2–8.8 times random. There are no dominant correlations between the hardness and the grain size or the hardness and microtexture. However, the hardest alumina coatings have $[1 0 \bar{1} 4]$ orientation texture and small grain sizes. The hardest TiC_xN_{1-x} coatings have a small grain sizes, [1 1 2] texture, and a high density of twins.

Acknowledgement

This work was supported primarily by Kennametal Inc. and the Pennsylvania DCED. Partial support by the MRSEC program of the National Science Foundation under Award Number DMR-0520425 is also acknowledged.

References

[1] Prengel HG, Pfouts WR, Santhanam AT. State of the art hard coatings for carbide cutting tools. Surf Coat Tech 1998;102:183–90.
[2] Quinto DT. Mechanical property and structure relationships for hard coatings for cutting tools. J Vac Sci Technol A 1988;6:2149–57.
[3] Lenander A, Akesson L. Coated cutting tool. European Patent EP0678594, 1999.
[4] Larsson A, Ruppi S. Microstructure and properties of Ti(C, N) coatings produced by moderate temperature chemical vapour deposition. Thin Solid Films 2002;402:203–10.
[5] Ruppi S. Deposition, microstructure and properties of texture-controlled CVD α-Al_2O_3 coatings. Int J Refract Met H 2005;23:306–16.
[6] Fallqvist M, Olsson M, Ruppi S. Abrasive wear of texture-controlled CVD α-Al_2O_3 coatings. Surf Coat Tech 2007;202:837–43.
[7] Ruppi S, Larsson A, Flink A. Nanoindentation hardness, texture and microstructure of α-Al_2O_3 and κ-Al_2O_3 coatings.. Thin Solid Films 2007;516:5959–66.
[8] Blendell JE, Vaudin MD, Fuller Jr ER. Determination of texture from individual grain orientation measurements. J Am Ceram Soc 1999;82:3217–20.
[9] Brandon DG. The structure of high angle grain boundaries. Acta Meter 1966;14:1479–84.

[10] Saylor DM, El-Dasher BS, Adams BL, Rohrer GS. Measuring the five parameter grain boundary distribution from observations of planar sections. Met Mater Trans 2004;35A:1981–9.
[11] Rohrer GS, Saylor DM, El-Dasher BS, Adams BL, Rollett AD, Wynblatt P, The distribution of internal interfaces in polycrystals. Z Metal 2004;95:197–214.
[12] The program can be down loaded at <http://rsb.info.nih.gov/ij/>.
[13] TestWorks 4 Software for Nanoindentation Systems Manual.
[14] Vedula VR, Glass SJ, Saylor DM, Rohrer GS, Carter WC, Langer SA, et al. Residual-stress Predictions in Polycrystalline Alumina. J Am Ceram Soc 2001;84:2947–54.
[15] Kim CS, Massa TR, Rohrer GS. Modeling the influence of orientation texture on the strength of WC–Co composites. J Am Ceram Soc 2007;90:199–204.
[16] Randle V. Twinning-related grain boundary engineering. Acta Mater. 2004;52:4067–81.